Materials Horizons

ROYAL SOCIETY OF CHEMISTRY

COMMUNICATION

View Article Online
View Journal | View Issue

Cite this: *Mater. Horiz.*, 2024, 11, 5274

Received 29th June 2024,
Accepted 12th August 2024

DOI: 10.1039/d4mh00831f

rsc.li/materials-horizons

A high-temperature-triggered crosslinking reaction to achieve excellent intrinsic flame retardancy of organic phase change composites†

Jingkai Liu, *[a] Yunyun Xiao,[c] Yiqing Wang,[a] Yishun Wuliu,[a] Xinbei Zhu,[ab] Liyue Zhang[a] and Xiaoqing Liu *[a]

The host–guest composite that integrates a porous scaffold and organic phase change materials (PCMs) features high energy density and customizable function, promising for advanced thermal storage/utilization. However, highly flammable organic PCMs are prone to severe combustion in porous structures, making it challenging for traditional flame-retardant methods to balance fire safety and latent heat. Herein, a high-temperature-triggered crosslinking reaction between the host and guest is designed using a polybenzoxazine-based aerogel (PB-1) and benzoxazine-based PCMs (C-dad). At high temperatures, the ring-opening polymerization (ROP) of C-dad can be initiated by and reacted with the phenolic groups of PB-1 to form a polybenzoxazine copolymer monolith with an improved char yield and intrinsic low flammability and without using the typical flame-retardant components. This enables the obtained composite (PB-1/C-dad) to well balance latent heat (145.3 J g^{-1}), char yield (a char residue of 13.1% at 600 °C), and flame retardancy (a peak heat release rate of 231 W g^{-1}), outperforming the representative flame-retardant modified polymer/organic PCM complexes reported in the literature. This thermal-triggered mechanism allows PB-1/C-dad to be repeatedly and stably used within the working temperature and activates its flame retardancy when exposed to open flames. The proposed host–guest crosslinking strategy is believed to inspire the development of inherently nonflammable phase change composites for safer thermal management.

New concepts

The combination of porous hosts and organic phase change material guests enables the integration of thermal energy utilization and versatility, but it is generally flammable as the low carbonization of phase change materials and porous structures that promotes oxygen contact. Polymer flame-retardant technology has inspired the modification of host–guest phase-change composites in recent years, but the efficiency is usually limited due to the absence of host–guest cooperation, providing a significant challenge. In this study, we propose a high-temperature-triggered crosslinking reaction between the host and guest to achieve synergistic flame retardancy, which results in a thermoset monolith composed of the polybenzoxazine copolymer with an improved char yield and intrinsic flame retardancy and without the introduction of typical flame-retardant components. This heat-stimulated crosslinking changes the pyrolysis behavior of the composites, rather than being two relatively independent components. Meanwhile, this co-reaction lies dormant at operating temperature to ensure stable and efficient heat storage, contributing to a good balance between fire resistance and latent heat. Significantly, this strategy can be further upgraded by tailoring the precursors or molecules, which enables multi-energy conversion, advanced utilization, and high-density energy storage, promising for safer thermal management.

Introduction

Benefiting from the excellent storage capacity and physico-chemical stability of phase change materials (PCMs), organic solid–liquid PCMs such as paraffin, fatty acids, and polyethylene glycol have attracted a lot of attention.[1] These PCM guests can be encapsulated by a three-dimensional (3D) porous host to achieve leakage resistance,[2] upgraded functions,[3] and portable applications[4] and have become one of the key research directions. Especially, polymer-based porous materials, which feature easy processing, high specific strength, designability, and good compatibility, have shown great potential in the development of cutting-edge host–guest phase-change composites.[5,6] However, polymer matrices are generally combustible, and so are organic PCMs with low flash points. It will become more severe, considering that porous 3D frames can increase the oxygen contact area.[7] The hidden fire danger of phase change composites (PCCs) must be considered seriously to ensure the safe operation of energy storage terminals.

Modern flame-retardant technology for polymer modification provides key ideas to improve the fire resistance of this

[a] Key Laboratory of Advanced Marine Materials, Ningbo Institute of Materials Technology and Engineering (NIMTE) of the Chinese Academy of Sciences (CAS), Ningbo 315201, P. R. China. E-mail: liuxq@nimte.ac.cn
[b] University of Chinese Academy of Sciences, Beijing 100049, P. R. China
[c] International Institute for Innovation, Jiangxi University of Science and Technology, Nanchang 330013, P. R. China

† Electronic supplementary information (ESI) available. See DOI: https://doi.org/10.1039/d4mh00831f

kind of PCC, mainly including physical addition and chemical modification of flame-retardant function components.[8] These methods are widely put into practice in both porous hosts and organic PCM guests to improve their flame retardancy.[9,10] For porous materials, flame-retardant enhancement can be achieved by skeleton modification and surface assembly. Taking flame retardants,[11] nonflammable precursors,[12] or nanomaterials[13] as building blocks, these functional components can be chemically or physically embedded into the skeletons of the porous scaffold during the preparation process. Through post-treatment, these flame retardant elements can also be attached to the skeleton surface through impregnation,[14] deposition,[15] or wrapping.[16] The homogeneously dispersed flame-retardant components can enhance the fire resistance of the matrix and effectively prevent flame propagation.[17] However, the current flame-retardant modification does not change the porous structure of the host, which can still accelerate the contact of internal flammable PCMs with combustion-assisting gases.

As an alternative idea, the flame-retardant modification on organic guest PCMs has received increasing attention in recent years.[18–20] Most organic PCMs contain a large number of unsaturated carbon bonds, whose combustion mainly involves vigorous oxidation reactions in the gas phase, along with a violent exothermic process.[21] Accordingly, catalytic carbonization and hindering gas-phase chain reactions are two key factors in designing flame-retardant PCMs, with corresponding fire-resistant components including hydroxides,[22] phosphorus derivatives,[23] and nitroaromatic compounds.[24] However, the introduction of flame-retardant components inevitably reduces the effective ratio of the heat storage medium or interferes with the crystallization behavior of PCMs coming at the cost of a substantial decrease in energy storage density, not to mention the complex or toxic modification process. Additionally, coating the flame-retardant system as a protective barrier on the PCC is another solution with wide applicability.[25–27] However, apart from a significantly reduced unit latent heat, this kind of shield usually can only resist the first combustion and does not change the thermal degradation behavior of the internal materials.[28] Therefore, the currently reported flame-retardant modification strategies have not essentially overcome the flammability of the host or the guest (Fig. 1(a)), making it difficult to balance the energy storage density and the flame retardancy of host–guest PCCs. Developing an effective flame-retardant method that applies to organic PCMs/porous material complexes presents significant challenges.

In this work, a high-temperature-triggered crosslinking reaction between organic PCMs and porous materials was designed to achieve host–guest synergistic flame retardancy. Specifically, a benzoxazine monomer with long fatty chains (C-dad) was designed as an organic PCM, and a polybenzoxazine aerogel (PB-1) with rich phenolic groups was employed as the supporting material. Taking advantage of the ring-opening polymerization (ROP) of benzoxazine, PCCs (PB-1/C-dad) can form a thermoset monolith composed of polybenzoxazine with a high char yield and intrinsic flame retardancy at high temperatures, while maintaining stable and efficient heat storage at operating temperature (Fig. 1(b)). This heat-stimulated crosslinking reaction changes the pyrolysis behavior of the two components in the composite and achieves a unique synergistic flame-retardant mechanism. As a result, the obtained PB-1/C-dad exhibited a high char yield at 600 °C of 13.1% and a low peak heat release rate (pHRR) of 231 W g^{-1} when the PCM contents exceeded 85 wt%. More importantly, PB-1/C-dad can self-extinguish immediately after being ignited using a 1500 °C flame and maintain the latent flame retardancy after repetitive use. This work provides an alternative approach for the

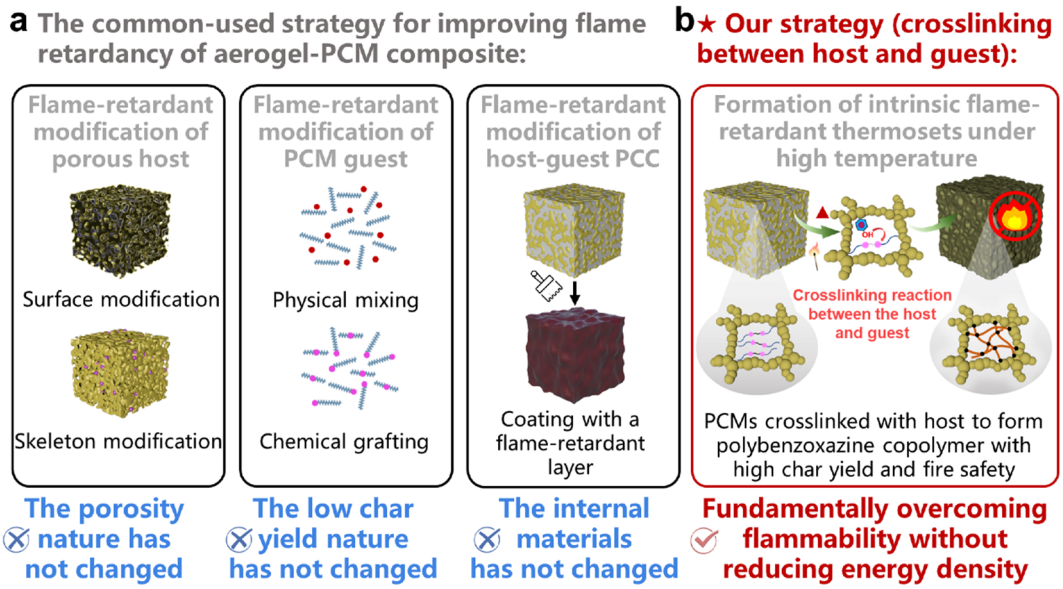

Fig. 1 Schematic of traditional flame-retardant methods of host–guest PCCs and the proposed flame-retardant mechanism in this study. (a) Flame-retardant modification of the porous host, PCM guest, and host–guest PCCs. (b) Designing the crosslinking reaction between the host and the guest to form intrinsic flame-retardant thermosets.

flame-retardant modification of host–guest PCCs on the premise of balancing energy density.

Results and discussion

Design principle of cross-linkable host–guest PCCs

For most host–guest PCCs, there is usually no synergistic flame-retardant effect between the supporting material and the PCM. Theoretically, it is feasible to design a smart synergistic effect for PCCs to efficiently balance the fire-retardant performance and the phase change behavior. Drawing inspiration from the fireproof thermosetting resins, such as the phthalonitrile resin,[29] phenolic resin,[30] and benzoxazine resin,[31] can be taken to form a 3D supporting material. In this work, we set out to design a cross-linking reaction between the host and the guest to endow the PCCs with the ability of thermal curing, which can be initiated when facing high temperatures or flames and produce a monolith material with a cross-linked structure and enhanced flame retardancy. The benzoxazine system was chosen for its unique curing behavior, molecular design flexibility, and intrinsic fire resistance. On the one hand, the ring-opening polymerization (ROP) of the benzoxazine resin can be triggered by heating, and the benzoxazine monomer can copolymerize with phenolic-containing chemicals.[32] On the other hand, a well-designed benzoxazine molecule is likely to possess both excellent phase change functions and thermosetting characteristics. We have previously synthesized a series of organic PCMs containing benzoxazine structures, which have tunable phase-change properties and can be cured to form polybenzoxazine at high temperatures.[33] The results also demonstrated that their flammability was significantly lower than commercial PCMs such as paraffin and fatty acids. Taking full use of the co-reaction between benzoxazine and phenolic-containing compounds, it is expected to obtain a cross-linkable host–guest PCC by integrating the phenolic-containing host and the benzoxazine-based PCM guest.

Targeting the synthesized phenolic-rich aerogel, we designed a pyrogallol-based benzoxazine precursor (PY-a) with two functional oxazines and one equivalent of the free phenolic group, as shown in Fig. 2(a). Through an HCl-catalyzed sol–gel process, PY-a can be transformed into porous aerogels (PB-1, PB-2, PB-3, and PB-4).[34,35] The 2-site phenolic group at the pyrogallol moieties combined with the newly formed phenolic groups after ROP contributes to an active skeleton surface rich in phenolic hydroxyls. Considering that the phenolic groups derived from the ring opening of oxazine are prone to form intramolecular 6-membered hydrogen bonds,[36] the free phenolic group attached to the pyrogallol unit ensures that the aerogel host has sufficient reactivity. In addition, three bifunctional benzoxazine monomers with long chain structures (abbreviated as C-dap, C-dah, and C-dad) were synthesized and directly used as organic PCMs. In their molecules, the two equivalent oxazine rings guarantee the crosslinking density after ROP, while the long-chain structure provides sufficient phase change enthalpy.

As illustrated in Fig. 2(c), the polybenzoxazine aerogel and the benzoxazine-based PCM were integrated through vacuum-assisted impregnation to obtain the PCC. Specifically, below the ROP

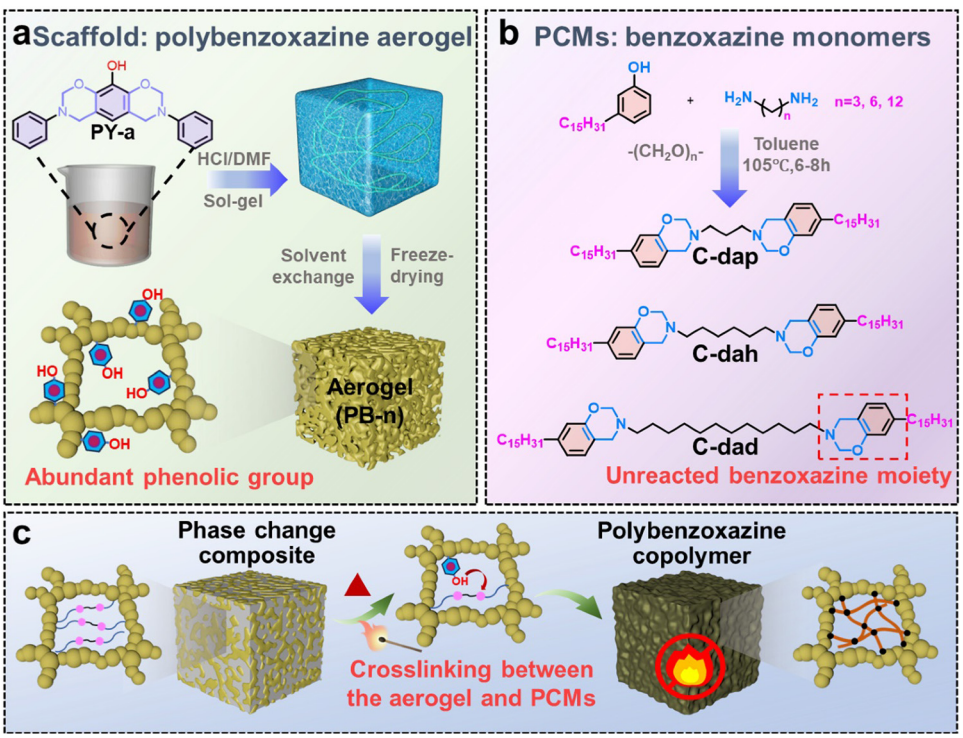

Fig. 2 Schematic illustration of the preparation of the host–guest PCC and its proposed flame retardancy mechanism. (a) Synthesis of the phenolic-rich aerogel by using PY-a. (b) Synthesis of benzoxazine-based PCMs. (c) Flame retardancy triggered by the crosslinking reaction between the aerogel and PCMs at high temperatures.

temperature, this PCC can stably and repetitively store/release latent heat. When the temperature reaches ROP, the benzoxazine monomer as the guest is cross-linked with the phenol-containing poly(PY-a) as the host, yielding a polybenzoxazine copolymer with an improved char yield and intrinsic flame retardancy. This mechanism will overcome the low charring ability of traditional organic PCMs and the severe burning caused by porous materials and change the pyrolysis behavior of the host and the guest, thereby achieving significant fireproof effects. It is also worth mentioning that the main starting materials involved in the synthesis process are bio-based chemicals, including pyrogallol, cardanol, and fatty diamines. Meanwhile, the one-step synthesis of monomers has a high yield, of which the main byproduct is water. Both the sustainable feedstocks and the high atom economy demonstrate their typical green chemical characteristics.

Synthesis and characterization of the benzoxazine-based aerogel and PCMs

All the benzoxazine monomers were prepared by the Mannich condensation reaction. In detail, PY-a as the aerogel precursor was synthesized from pyrogallol, aniline, and paraformaldehyde (Fig. S1, ESI†). The successful synthesis of PY-a was confirmed by ^{1}H nuclear magnetic resonance (NMR), ^{13}C NMR, Fourier transform infrared spectroscopy (FT-IR), and high-resolution mass spectrometry (HRMS), as shown in Fig. 3(a) and Fig. S2–S4 (ESI†). In Fig. 3(a), the signals observed at 5.43 and 4.57 ppm are attributed to O–CH_2–N and Ar–CH_2–N, respectively, and the peak located at 8.37 ppm belongs to the free phenolic group at the 2-site of the pyrogallol moiety. Furthermore, two typical absorbance bands related to the oxazine ring are found at 1067 and 978 cm^{-1}, which correspond to the asymmetric/symmetrical stretching vibration of Ar–O–C and the asymmetric stretching vibration of C–N–C, respectively, while the strong absorption peaks at ~3250 and 1355 cm^{-1} can be attributed to the free phenolic group (Fig. S3, ESI†). Additionally, the results of ^{13}C NMR and HRMS of PY-a benzoxazine monomers are consistent with their structure (Fig. S4, ESI†).

Catalyzed by hydrochloric acid, PY-a can undergo sol–gel transformation to form an organogel in the DMF solvent under mild conditions, which is further followed by solvent replacement

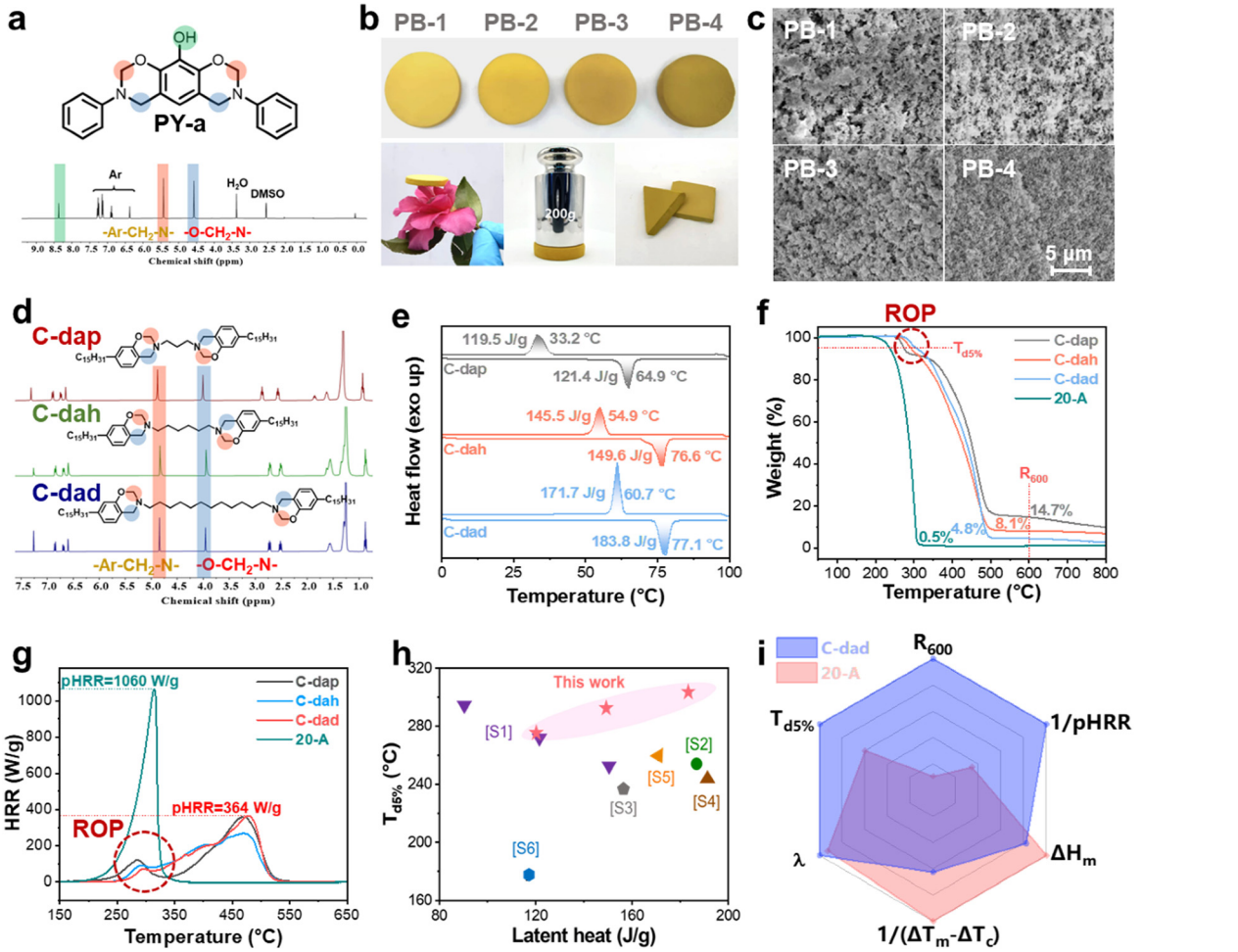

Fig. 3 (a) ^{1}H NMR spectrum of PY-a. (b) Digital photographs of the prepared polybenzoxazine-based aerogel and the illustration of its lightweight, pressure-resistant, and customizable shape. (c) SEM images of four aerogels. (d) ^{1}H NMR spectra of C-dap, C-dah, and C-dad. (e) DSC diagrams of three benzoxazine-based PCMs. TGA curves (f) and MCC results (g) of C-dap, C-dah, C-dad, and 20-A. (h) Literature comparison focused on $T_{d5\%}$ and latent heat. (i) Radar plots of C-dad and 20-A, in which the results are normalized by the maximum value of each aspect.

and ambient pressure drying processes to produce the poly(PY-a) aerogel. By regulating the concentration of precursor solution (2.8, 3.9, 4.8, and 7.1 wt%), four aerogel materials with different densities and porosities were obtained, which are named PB-1, PB-2, PB-3, and PB-4, respectively. Their digital photographs reflect gradually darker colors, corresponding to various densities (Fig. 3(b)). The FT-IR spectrum (Fig. S5, ESI†) indicates that the characteristic peak of the oxazine ring disappears, and the intensity of the hydroxyl absorption band increases simultaneously, implying the occurrence of the ROP reaction of PY-a. These aerogels exhibit typical features of lightweight, compression resistance, and tailorability, which can be placed on flowers, bear about 20 times their weight, and be molded into different sizes or shapes, as shown in Fig. 3(b). Meanwhile, the adsorption capacity provided by the porous structure allows it to be wetted by solvents with different polarities (Fig. S6, ESI†). With the increase of the mass fraction of precursor solution, the densities of aerogels increased from 0.140 to 0.323 g cm^{-3}, while the loading rate decreased from 83.6% to 65.4% due to the higher unit volume fraction of the skeleton (Fig. S7, ESI†). As revealed by SEM (Fig. 3(c)), polybenzoxazine aerogels display typical micro-nanoporous structures with a ''pearl necklace-type'' network due to the nanoparticle aggregation.[37] In detail, as the concentration of the precursor solution increases, both the skeleton size and the pore size of the aerogels decrease, signifying their descending porosities. In addition, the N_2 adsorption–desorption measurement (Fig. S8, ESI†) shows that the surface area (S_{BET}), total pore volume (V_t), and micropore volume (V_{micro}) follow a similar trend. It is noteworthy that the pore structure dominated by mesopores is beneficial for providing phase transition space for PCMs.[38] All the physical parameters of four aerogels are recorded in Table S1 (ESI†). Importantly, the highest specific surface area of PB-1 is 107.4 $m^2 g^{-1}$, which outperforms the typical polybenzoxazine-based aerogels reported in the literature.[39] These micro-nanoporous structures enable a sufficient capillary force and surface tension, ensuring the stable encapsulation of a large amount of organic PCMs.

Following the same synthesis procedure, we prepared three bifunctional benzoxazine monomers with long-chain structures using cardanol, fatty diamines, and polyformaldehyde (Fig. S9, ESI†). According to the type of diamine sources (1,3-diaminopropane, 1,6-diaminohexane, and 1,12-diaminododecane), they are respectively named C-dap, C-dah, and C-dad. Their chemical structures were also confirmed by ^{1}H NMR, ^{13}C NMR, FT-IR, and HRMS, and the corresponding spectra are shown in Fig. 3(d) and Fig. S10–S14 (ESI†). As illustrated in Fig. 3(d), the diagnostic signals of the oxazine ring (O–CH_2–N and Ar–CH_2–N) can be observed at ~4.86 and ~3.99 ppm in ^{1}H NMR, respectively, while the peaks between 0.79 and 1.91 ppm are related to the hydrocarbon groups. Detailed chemical shifts and integrals are recorded in the Experimental section, demonstrating the successful synthesis of three monomers. Notably, unlike PY-a, there is no absorption band of hydroxyl in the results of FT-IR (Fig. S10, ESI†). Meanwhile, the characteristic signals of benzoxazine are located at 1084 and 938 cm^{-1}. Additionally, the corresponding signals in ^{13}C NMR and the exact molecular ion peaks in HRMS strongly support the correct structure of the target product (Fig. S12–S14, ESI†).

Benefiting from the long-chain groups, C-dap, C-dah, and C-dad exhibit excellent phase transition performance, as evaluated by DSC (Fig. 3(e) and Table S2, ESI†). Specifically, the melting temperatures (T_m) of C-dap, C-dah, and C-dad are 64.9, 76.6, and 77.1 °C, respectively, with corresponding melting enthalpies (ΔH_m) of 121.4, 149.6, and 183.8 J g^{-1}. The high latent heat of C-dad indicates that the influence of the oxazine ring on the phase change of the molecule is relatively small. Meanwhile, their supercooling degrees are calculated as 31.7, 21.7, and 16.4 °C based on the difference between T_m and the crystallization temperature (T_c), in which the value of C-dad is comparable to that of the typical organic PCMs.[40] It is obvious that the phase-change temperature and enthalpy increase with the increasing diamine length, mainly due to the stronger intermolecular van der Waals forces caused by molecular chain elongation.[41] The T_m of C-dah and C-dad are similar, which is attributed that the contribution of molecular chain elongation to entropy gradually decreases.[42] Importantly, the phase-change behavior of the three monomers remained almost unchanged after fifty cycles, indicating their good thermal reliability (Fig. S15–S17, ESI†). Under the same testing conditions, the commercial fatty acids (eicosoic acid, abbreviated as 20-A) with similar fusion points exhibit a melting enthalpy of 210.6 J g^{-1} and a supercooling degree of 10.3 °C (Fig. S18, ESI†). X-ray powder diffraction (XRD) patterns present the difference in crystal structures (Fig. S19, ESI†), in which the typical polymorphic forms can be observed. The crystallinities of C-dap, C-dah, and C-dad were calculated as 65.75, 72.95, and 93.99%, respectively. Accordingly, the elongation of the diamine moiety is considered to increase the ability of benzoxazine monomers to pack and form ordered crystals. Similarly, polarized optical microscopy (POM) reveals the crystal morphologies of three monomers, in which the cross-extinction patterns with spherulitic crystals can be observed (Fig. S20, ESI†). Especially, C-dad displays the smallest crystal size due to the elongation of molecules promoting the free movement, which is consistent with its highest thermal enthalpy. The thermal conductivity (λ) was also evaluated (Fig. S21, ESI†), and the slightly higher λ of the benzoxazine-based PCMs may be due to an increase in intermolecular forces in the presence of polar heteroatoms.[43] Further measurement of thermal stability was conducted by thermogravimetric analysis (TGA). As shown in Fig. 3(f), as the carbon number of diamine increases, the 5% thermal decomposition temperature ($T_{d5\%}$) of the benzoxazine-based PCMs gradually increases. The possible reason is that the ROP reaction will lead to the fracture of active species and the volatilization of fragments.[44] The DSC results indicate that the peak temperatures of ROP of C-dap, C-dah, and C-dad are 230.8, 262.9, and 266.7 °C, respectively (Fig. S22, ESI†). The increase in temperature required for ROP delays the occurrence of this thermal degradation, as proved by the TGA–DSC curves (Fig. S23–S25, ESI†). In TGA results, the first thermal degradation stage can be assigned to the occurrence of ROP,[45] which is labeled by a red cycle. Furthermore, it can be observed that an increase in the proportion of hydrocarbon groups will lead to a decrease in the char yield at 600 °C (R_{600}) and 800 °C (R_{800}).

Interestingly, the R_{600} values of C-dap, C-dah, and C-dad are as high as 14.7, 8.1, and 4.8%, respectively. In contrast, 20-A has already been completely decomposed before 310 °C. The good char-forming ability is attributed to the occurrence of ROP and the formation of cross-linked polybenzoxazine.

Benefiting from the self-curing behavior of three benzoxazine-based PCMs at high temperatures, it can be expected that the formation of polybenzoxazine will also lead to an enhancement in flame retardancy. The combustibility of synthesized PCMs and 20-A was evaluated using microscale combustion calorimetry (MCC) (Fig. 3(g)). It is obvious that 20-A is highly flammable, reflected by its lowest maximum heat release temperature of 315 °C and the highest pHRR of 1060 W g^{-1}. By comparison, the maximum heat release temperature of the benzoxazine monomer is decreased to 479 °C, and the pHRR of C-dad is also as low as 364 W g^{-1}. The excellent flame resistance is mainly attributed to the intrinsic flame retardancy of the formed polybenzoxazine at high temperatures. As marked by a red circle in Fig. 3(g), the small peaks are believed to be the heat release caused by the escape of small molecules during ROP. Significantly, compared to the reported synthesized organic PCMs with typical flame-retardant groups such as the phosphorus element and nitroaromatic groups, the devised benzoxazine-based PCMs well balance flame retardancy and thermal storage density (Fig. 3(h) and Table S3, ESI†). Besides, the total heat release (THR) values based on MCC of C-dap, C-dah, C-dad, and 20-A are 40.2, 39.7, 42.2 and 41.2 kJ g^{-1} (Fig. S26, ESI†), respectively. Although they are similar due to the high contents of long-chain alkyl groups, the significantly lower pHRRs of benzoxazine-based PCMs can effectively suppress early intense combustion. To further highlight the advantages of C-dad as a PCM, we compared its thermal stability, flame retardancy, thermal conductivity and phase-change performance with 20-A. As displayed in Fig. 3(i), C-dad possesses lower latent heat and higher supercooling degree than 20-A, but its thermal stability and fire resistance are significantly better, which serves as a promising substitute for hydrocarbon-based PCMs, especially for some high safety requirements of applications.

Fabrication of the PCC and its flame retardancy

Considering its excellent thermal storage capacity, C-dad was selected as the PCM for further investigation. Meanwhile, PB-1 with a high encapsulation rate and a suitable pore size was chosen as the supporting material to ensure excellent energy storage density. A representative PCC sample was further prepared using a vacuum-assisted infiltration method and named PB-1/C-dad. SEM reveals that most of the pores of PB-1 have been filled with C-dad (Fig. 4(a)), implying the good capillary force and interface compatibility offered by the host. The tight integration of PB-1 and C-dad also makes it appear dark brown macroscopically, as shown in the digital photograph in Fig. 4(a). Meanwhile, FT-IR spectra demonstrate that there are only physical interactions between PB-1 and C-dad instead of chemical reactions (Fig. S27, ESI†). The loading rate of PB-1/C-dad is as high as 83.6 wt%, which is calculated by the weight difference before and after encapsulation (eqn (S1), ESI†). DSC was conducted to measure the phase change performance of PB-1/C-dad, as portrayed in Fig. 4(b). Compared with pure C-dad, the latent heat of the PCC decreases to 145.3 J g^{-1}, as the aerogel scaffold does not contribute to the thermal energy storage. The supercooling degree of PB-1/C-dad was measured to be 17.3 °C, which is slightly higher than that of C-dad. Meanwhile, the phase-change temperature of PB-1/C-dad is slightly lower than that of C-dad, possibly attributed to the negative influence of the micropore and interface interaction on the phase transition behavior of PCMs.[46] In XRD patterns (Fig. S28, ESI†), it can be observed that PB-1, as a polymeric material, exhibits a typical amorphous structure, and the crystallinity of PB-1/C-dad also decreases to some extent. However, the crystallization efficiency of PB-1/C-dad is calculated to be as high as 94.6% using eqn (S2) (ESI†), which is comparable to most reported aerogel/organic PCMs complexes.[47,48] To demonstrate the leakage-proof properties of PB-1/C-dad, both PB-1/C-dad and pure C-dad were placed on a heating stage. As shown in Fig. 4(c), by procedurally heating at 20, 40, 60, 80, and 100 °C for 60 s each, it can be observed that C-dad melted at 80 °C and became flowable, which corresponds to its fusion point, resulting in a heavily draining at 100 °C. In contrast, PB-1/C-dad exhibited good shape stability and can resist the leakage of the inner PCMs even above the melting temperature. The anti-leakage performance of PB-1/C-dad is further supported by mass-time variation curves, which present almost no mass loss after continuous heating in a 150 °C oven for 600 min (Fig. 4(d)). Besides, the TGA curve of the phase-change composite (Fig. S29, ESI†) indicates that its $T_{d5\%}$ and maximum thermogravimetric temperature are 288.2 and 474.4 °C, respectively, corresponding to its high thermal stability. Both the good leakage resistance and the thermal stability allow it to complete 50 cycles easily without changing the thermal storage capacity and the crystal structure (Fig. S30 and S31, ESI†). It is also worth noting that the dark brown color of PB-1/C-dad also endows it with intrinsic photothermal conversion ability. Under 2 units of the simulated sunlight, PB-1/C-dad can undergo phase transition within 500 s and eventually achieve a maximum temperature of ~90 °C (Fig. 4(e)). According to eqn (S3) and Fig. S32 (ESI†), the photothermal conversion efficiency of PB-1/C-dad is estimated to be 89.3%. The excellent thermal durability and intrinsic light energy utilization ability make it a promising thermal storage material.

To evaluate the flame retardancy of PB-1/C-dad, an appropriate amount of sample was placed in a crucible and burned using a 1500 °C flame spray gun, of which the combustion behavior was recorded (Fig. 4(f) and Movie S1, ESI†). As a comparison, 20-A and its PCC prepared using PB-1 (PB-1/20-A) were also burned under the same conditions (Movie S2, ESI†). Specifically, PB-1/C-dad successively underwent melting, curing, and charring after ignition, and formed high-yield and relatively complete chars within 15 s. After removing the flame, PB-1/C-dad self-extinguished immediately, and a large amount of carbon residues remained. More intuitively, after igniting a block of PB-1/C-dad for 10 s, both a self-extinguishing phenomenon and a noticeable carbon layer appeared (Fig. S33, ESI†).

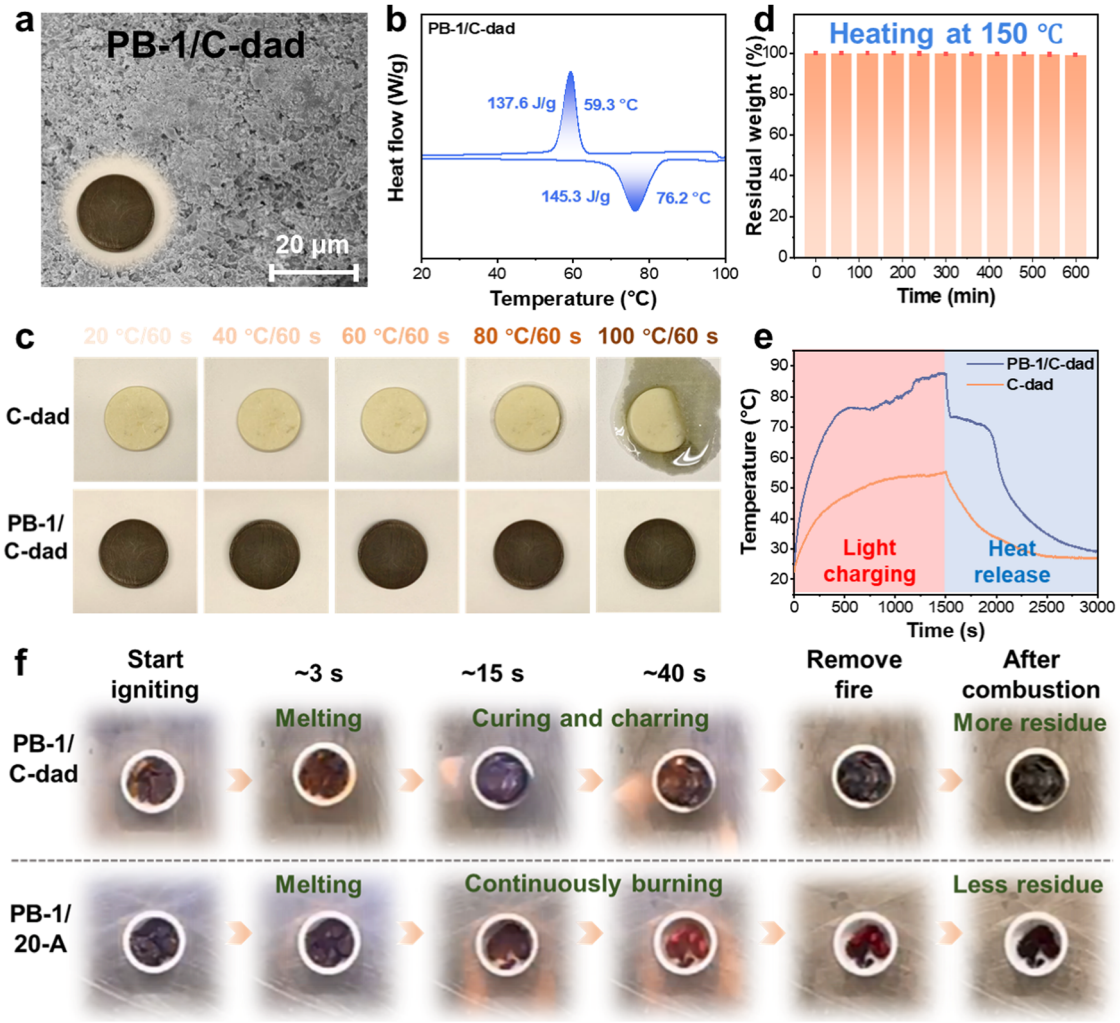

Fig. 4 (a) SEM and a digital photograph of PB-1/C-dad. Thermal storage performance of PB-1/C-dad: (b) DSC diagram, (c) form stability, (d) weight variation when heating at 150 °C, and (e) intrinsic photothermal conversion ability. (f) Combustion tests of PB-1/C-dad and PB-1/20-A.

In contrast, there was intense combustion in PB-1/20-A, which continued to burn after removing the flames, ultimately produced only a small amount of char residues. It can be anticipated that, in the MCC results (Fig. S34, ESI†), PB-1/20-A also shows a significantly higher pHRR (744 *vs.* 231 W g^{-1}) and THR (38.3 *vs.* 31.5 kJ g^{-1}) than PB-1/C-dad. To further highlight the flame-retardant ability of the designed system, the combustion behaviors of C-dad, 20-A, and PB-1 were also investigated (Fig. S35, ESI†). Specifically, the synthesized benzoxazine-based PCM has good intrinsic fire resistance, which completed melting and ROP within 15 s. However, 20-A was burned out within 12 s after ignition, with almost no residual carbon formed. The ROP behavior of C-dad is proved by FT-IR (Fig. S36, ESI†), in which the sample heated from room temperature to 300 °C exhibited typical characteristics of polybenzoxazine. The production of polybenzoxazine is beneficial for further improved flame retardancy and char yield rate, and eventually achieves self-extinguishing and generates carbon residues.[33] It can be expected that PB-1, as a polybenzoxazine material, has good inherently low flammability and could rapidly transform into char products that act as a protective barrier.[49] In summary, PB-1/C-dad has good fireproof ability and high char-forming ability when exposed to fire, which is expected to enlighten the solution of the flammability problem of traditional organic PCMs in porous materials.

High-temperature-triggered crosslinking between the host and the guest

To reveal the reasons for the intrinsic flame retardancy of PB-1/C-dad, the crosslinking reaction of PB-1/C-dad was studied. Temperature evolutions during actual combustion were simulated by setting a rapid heating rate (20 °C min^{-1}) in DSC. As shown in Fig. 5(a), pure C-dad and PB-1/C-dad present exothermic peaks at 288.7 and 219.4 °C, respectively, demonstrating that the ROP reactions occurred. The significantly reduced ROP temperature and exothermic enthalpy of PB-1/C-dad serve as the typical characteristics of a catalytic ROP.[49] Theoretically, the ROP of the benzoxazine monomer can be catalyzed by acidic phenolic groups, and the proton generated by the dissociation of phenolic groups can combine with the

oxygen atom of the oxazine ring to form an oxonium ion, thereby reducing the ring-opening energy barrier of the oxazine ring, which is a cationic catalytic mode.[50] Meanwhile, the phenolic moiety can act as a nucleophilic species to attack the electrophilic substitution reaction sites in benzoxazine monomers, producing adducts or polymers.[51] Under the combined effect of two mechanisms, C-dad and PB-1 can crosslink with each other, thereby reducing the ROP temperature of C-dad and leading to the formation of polybenzoxazine copolymers, *i.e.* poly(C-dad)-*co*-poly(PY-a). To further validate this crosslinking reaction, PB-1/C-dad was heated at 220 °C for 2 hours to obtain the cured PB-1/C-dad, and its chemical structure was detected by FT-IR. Compared to the uncured PB-1/C-dad, the characteristic peak of benzoxazine disappears in the spectrum of the cured PB-1/C-dad (Fig. S37, ESI†). Instead, the intensity of the phenolic hydroxyl absorption band increases, corresponding to the occurrence of ROP. Additionally, as shown in Fig. 5(b), pure PB-1 exhibits strong peaks standing for the penta-substituted benzene at 870 cm^{-1}, while the cured PB-1/C-dad shows obvious tetra-substituted benzene (822 cm^{-1}) and hexa-substituted benzene (1620 cm^{-1}).[52,53] Among them, the signal of the tetra-substituted benzene is due to the substitution of the aromatic-H in C-dad by nucleophilic species, while the signal of the hexa-substituted benzene ring corresponds to the substitution reaction between the penta-substituted benzene moiety in poly (PY-a) and C-dad. More importantly, after being thermally treated at 270 °C for 2 hours, the gel contents of PB-1, C-dad, and PB-1/C-dad were measured to be 96.48%, 97.14%, and 97.74%, respectively. PB-1 and the cured C-dad as polybenzoxazine materials display high gel fractions, corresponding to their cross-linked network structures. Interestingly, the thermal-treated PB-1/C-dad has the highest gel content, which is likely related to the host–guest crosslinking reaction further increasing the crosslinking density, instead of an individual curing reaction of C-dad. Therefore, there is a crosslinking reaction between PB-1 and C-dad at high temperatures, which transforms the small molecules and poly(PY-a) into a bulk copolymer with increased

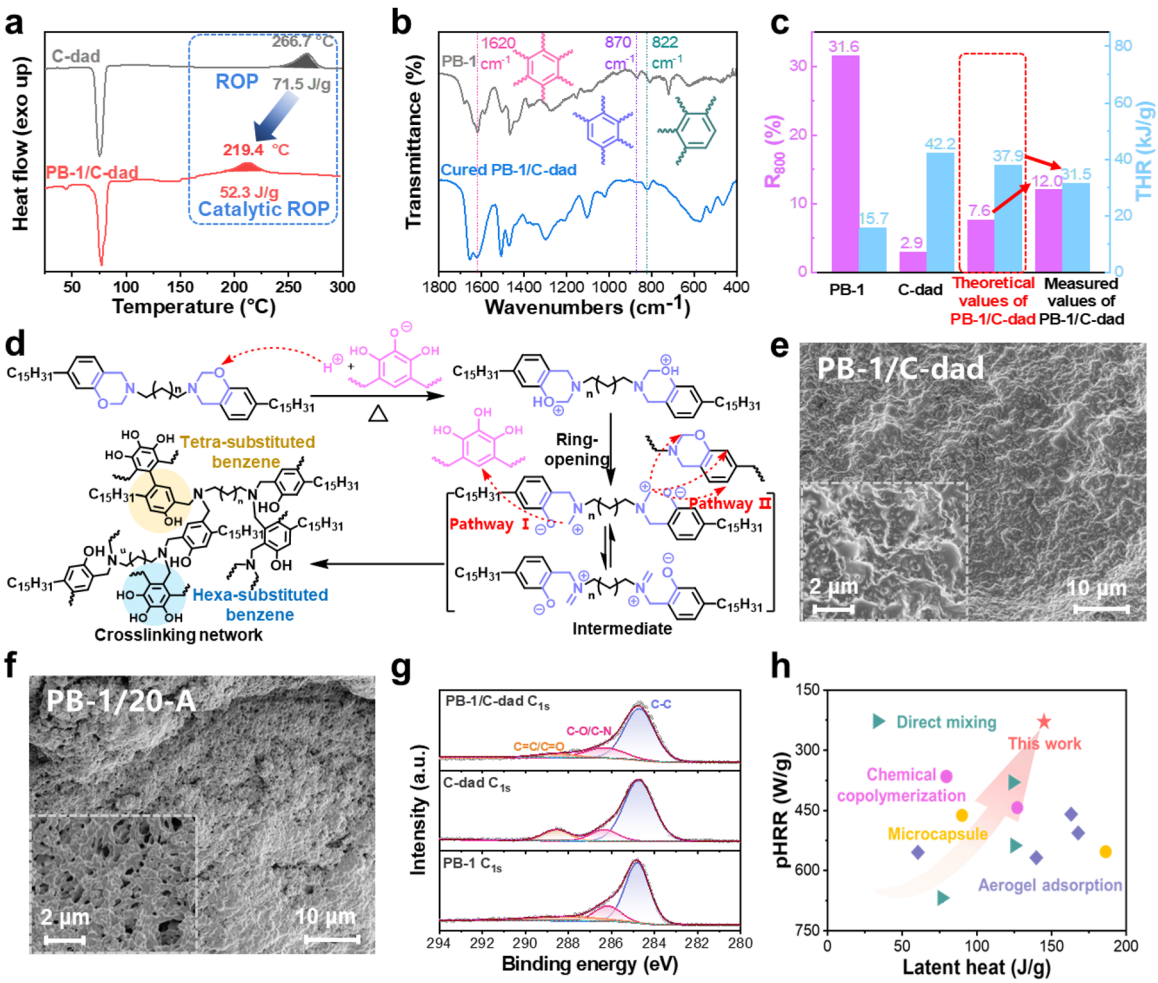

Fig. 5 (a) ROP behaviors of C-dad and PB-1/C-dad based on DSC. (b) FT-IR spectrums of PB-1 and the cured PB-1/C-dad. (c) Comparison of the theoretical values and measured values of R_{800} and THR of PB-1/C-dad. (d) The proposed mechanism of the crosslinking reaction between C-dad and poly(PY-a). SEM images of the char layers: PB-1/C-dad (e) and PB-1/20-A (f). (g) C_{1s} spectrums of the char residues of PB-1/C-dad, C-dad, and PB-1. (h) Comparison of the pHRR and latent heat of PB-1/C-dad with the representative polymer/organic PCM composites in the previous literature.

crosslinking density, thereby significantly improving char-forming ability and flame retardancy.

Targeting further demonstration of the effect of the crosslinking reaction on flame retardancy, we tested the char yield and flammability of C-dad, PB-1, and PB-1/C-dad by TGA and MCC (Fig. S38 and S39, ESI†). In theory, if there is no synergistic effect between PB-1 and C-dad, the char yield of PB-1/C-dad will be close to the weighted sum of the respective char yield of PB-1 and C-dad based on their mass fraction, which is defined as the theoretical value. Fig. 5(c) summarizes the results of TGA and MCC. The char yields at 800 °C (R_{800}) of C-dad, PB-1, and PB-1/C-dad were 2.9, 31.6, and 12.0%, respectively. The theoretical R_{800} of PB-1/C-dad calculated by the weighted sum (eqn (S4), ESI†) is 7.3%, significantly lower than its measured value of 12.0%. In addition, the THR values of C-dad, PB-1, and PB-1/C-dad investigated by MCC are 42.2, 15.7, and 31.5 kJ g^{-1}, respectively. The weighted sum of THR values of C-dad and PB-1 calculated using eqn (S5) (ESI†) is 37.9 kJ g^{-1}, which is also higher than its measured value. The remarkable improvements are attributed to the crosslinking reactions between PB-1 and C-dad, which transform small-molecular PCMs into macro-molecular copolymers.

Based on the above analysis, the mechanism of the high-temperature-triggered crosslinking reaction is proposed in Fig. 5(d). Specifically, the abundant phenolic hydroxyl groups on the surface of the aerogel skeleton dissociate at high temperatures to produce protons and initiate the cationic catalytic ROP of C-dad. Subsequently, the protonated benzoxazine monomers undergo ring opening to form zwitterionic intermediates. These active species can react with the 5-site of the pyrogallol moiety in poly(PY-a) to obtain hexa-substituted benzene linkage (pathway I), as well as with O–CH_2–N in C-dad and the unsubstituted 2- and 4-sites in the phenyl group to yield the tetra-substituted benzene linkage (pathway II). Eventually, the reaction is complete, a polybenzoxazine copolymer with a crosslinked network yield, thereby changing the pyrolysis behavior of the original PCC and improving charring ability as well as fire resistance. Significantly, this ROP reaction can still occur after 50 cycles, as reflected in the exothermic peak at ~220 °C in the DSC result (Fig. S40, ESI†), indicating that its safety can still be maintained after long-time service. The crosslinking reaction between the benzoxazine-based PCM and polybenzoxazine-based aerogel can be regarded as a "thermal-triggered switch", which lies dormant at low temperatures to ensure the normal operation, while at high temperatures it can spontaneously cure to form intrinsic flame-retardant polymer materials, and the schematic illustration is presented in Fig. 2(c).

Generally speaking, the intrinsic flame retardancy of polybenzoxazine is attributed to hydroxyl groups, tertiary amine, and benzene groups with high molar group contributions.[54] On this basis, high-quality and high-yield char layers help further improve the fire-proof efficiency in the condensed phase. Accordingly, the morphology and chemical structure of the carbon residues of PB-1/C-dad after combustion were studied by SEM and X-ray photoelectron spectroscopy (XPS). As shown in Fig. 5(e), a continuous and dense carbon layer was formed on the surface of the burned PB-1/C-dad. An energy dispersive spectrometer further reveals its chemical composition dominated by carbon elements (Fig. S41, ESI†). This high-quality char layer is beneficial for isolating heat and oxygen, preventing the release of combustible fragments, and protecting internal materials from further combustion. In contrast, the char layer of PB-1/20-A after combustion exhibits a typically loose and porous structure (Fig. 5(f)), indicating that the flammable 20-A has been almost burned out. This porous carbon layer will further intensify the combustion of internal PCMs, which is consistent with its combustion experiment results. The chemical structure of the residual carbon was further analyzed by XPS (Fig. S42, ESI†). As shown in Fig. 5(g), the C_{1s} spectrums indicate that the char residues of the combusted samples are mainly composed of C–C at 284.0 eV, C–O/C–N at 285.2 eV, and C=C at 288.4 eV.[55,56] The cross-linked network predominantly composed of aromatic C–C makes an important contribution to the fire resistance of PB-1/C-dad, which is similar to the literature results.[57] In addition, compared to PB-1 and C-dad, PB-1/C-dad has more content of C–C and less content of sp^2 C (Fig. S43, ESI†), which supports the synergistic effect of PB-1 and C-dad in PCCs.

This synergistic flame-retardant mechanism based on a crosslinking reaction well balances energy storage density and anti-flammability. To highlight the advantages of PB-1/C-dad in the aspects of thermal storage and flame retardancy, both melting latent heat (145.3 J g^{-1}) and pHRR of PB-1/C-dad (231 W g^{-1}) are compared with the literature that integrates the polymeric matrix and organic PCMs by different methods (Table S4, ESI†). As illustrated in Fig. 5(h), although most of these reports used flame retardants or nanoadditives, the melting enthalpy and pHRR of PB-1/C-dad still outperform those reported results. Compared to the research results, PB-1/C-dad simultaneously possesses high R_{600} and low pHRR (Fig. S44 and Table S4, ESI†), albeit some studies have used macromolecular polyethylene glycol as organic PCMs. Significantly, this strategy does not have to introduce flame-retardant components like the traditional method. More importantly, the system designed in this study can be further upgraded by optimizing the chemical structure or customizing the aerogel. For example, benzoxazine monomers can be synthesized as monofunctional, bifunctional, and trifunctional molecules, of which the molecular symmetry can also be regulated by designing different molecules. For the aerogel host, in theory, the polymeric aerogel with *ortho*- and *para*-unsubstituted phenolic groups can crosslink with benzoxazine-based PCMs, such as the phenolic resin aerogel, polyimide aerogel, *etc.*

Conclusions

We report a scaffold-PCM crosslinking strategy based on the co-reaction between a benzoxazine-based PCM and a polybenzoxazine-based aerogel, which successfully addresses the poor charring ability of organic PCMs and low flame-retardant synergy between the host and the guest. The devised PB-1/C-dad PCC exhibits an excellent thermal storage density of 145.3 J g^{-1}, a high R_{600} of 13.1%, and a low pHRR of 231 W g^{-1}. By simulating combustion

and thermal runaway processes, it has been proven that the phenolic group of PB-1 can trigger the ROP of C-dad, resulting in a polybenzoxazine copolymer monolith with a cross-linked structure. The combustion experiment shows that PB-1/C-dad can quickly form a dense carbon layer when being ignited, thereby playing a barrier role in the condensed phase. This flame-retardant mechanism based on the high-temperature-triggered crosslinking reaction effectively balances latent heat and fire resistance without chemically introducing flame-retardant groups or physically blending flame retardants while ensuring long-term stability. Moreover, this strategy can be further upgraded by tailoring the aerogel precursors or PCM molecules to meet the needs of multi-energy conversion and advanced utilization, which will inspire new ways of flame-retardant enhancement of the host–guest phase-change composites.

Author contributions

Conceptualization and methodology: J. K. Liu and X. Q. Liu. Formal analysis: J. K. Liu, X. Q. Liu, and Y. Q. Wang. Software and visualization: J. K. Liu, Y. Y. Xiao, Y. S. Wuliu, and X. B. Zhu. Investigation: J. K. Liu, Y. Y. Xiao, Y. Q. Wang, Y. S. Wuliu, L.Y. Zhang, and X. B. Zhu. Writing – original draft: J. K. Liu. Writing – review and editing: X. Q. Liu, J. K. Liu, and X. B. Zhu. Supervision, project administration, resources, and funding acquisition: X. Q. Liu.

Data availability

The data that support the findings of this study are available from the corresponding author upon reasonable request.

Conflicts of interest

There are no conflicts to declare.

Acknowledgements

The authors are grateful for the financial support from the National Key R&D Program of China (2023YFB3709700), the National Natural Science Foundation of China (U23A20589 and 52003283), the China Postdoctoral Science Foundation (2022M723250), The Zhejiang Provincial Natural Science Foundation (LQ24E030014), the Ningbo 2025 Key Scientific Research Programs (2022Z111, 2022Z160, and 2022Z198), the Natural Science Foundation of Ningbo City (2022J302), and The Leading Innovative and Entrepreneur Team Introduction Program of Zhejiang (grant no. 2021R01005).

References

1 G. Wang, Z. Tang, Y. Gao, P. Liu, Y. Li, A. Li and X. Chen, *Chem. Rev.*, 2023, **123**, 6953–7024.
2 X. Li, G. Dong, Z. Liu and X. Zhang, *ACS Nano*, 2021, **15**, 4759–4768.
3 J. Lyu, Z. Sheng, Y. Xu, C. Liu and X. Zhang, *Adv. Funct. Mater.*, 2022, **32**, 2200137.
4 S. Liu, B. Quan, M. Sheng, Y. Yang, X. Hu, C. Zhu, X. Lu and J. Qu, *Nano Energy*, 2023, **114**, 108669.
5 P. Liu, X. Chen, Y. Li, P. Cheng, Z. Tang, J. Lv, W. Aftab and G. Wang, *ACS Nano*, 2022, **16**, 15586–15626.
6 C. Liu, T. Xiao, J. Zhao, Q. Liu, W. Sun, C. Guo, H. M. Ali, X. Chen, Z. Rao and Y. Gu, *Renewable Sustainable Energy Rev.*, 2023, **188**, 113814.
7 Y. Yang, J. Lyu, J. Chen, J. Liao and X. Zhang, *Adv. Funct. Mater.*, 2021, **31**, 2102232.
8 B. W. Liu, H. B. Zhao and Y. Z. Wang, *Adv. Mater.*, 2022, **34**, e2107905.
9 Z. M. Png, X. Y. D. Soo, M. H. Chua, P. J. Ong, A. Suwardi, C. K. I. Tan, J. Xu and Q. Zhu, *Sol. Energy*, 2022, **231**, 115–128.
10 K. Pielichowska, N. Paprota and K. Pielichowski, *Materials*, 2023, **16**, 4391.
11 H. Yi, L. Xia and S. Song, *Compos. Sci. Technol.*, 2022, **217**, 109121.
12 Z. Yu, Y. Wan, Y. Qin, Q. jiang, J.-P. Guan, X.-W. Cheng, X. Wang, S. Ouyang, X. Qu, Z. Zhu, J. Wang and H. He, *Chem. Eng. J.*, 2023, **477**, 147187.
13 Y. Zhou, W. Liu, S. Zhang, H. Liu, Z. Wu and X. Wang, *ACS Appl. Mater. Interfaces*, 2024, **16**, 7754–7767.
14 H. Yue, Y. Ou, J. Wang, H. Wang, Z. Du, X. Du and X. Cheng, *Energy*, 2024, **286**, 129441.
15 H. Yue, J. Wang, H. Wang, Z. Du, X. Cheng and X. Du, *ACS Appl. Mater. Interfaces*, 2023, **15**, 8093–8104.
16 Y. Chen, Y. Meng, J. Zhang, Y. Xie, H. Guo, M. He, X. Shi, Y. Mei, X. Sheng and D. Xie, *Nano-Micro Lett.*, 2024, **16**, 196.
17 J. Shen, P. Zhang, L. Song, J. Li, B. Ji, J. Li and L. Chen, *Composites, Part B*, 2019, **179**, 107545.
18 R. Chen, X. Huang, R. Zheng, D. Xie, Y. Mei and R. Zou, *Chem. Eng. J.*, 2020, **380**, 122500.
19 Y. Wang, L. Zhao, W. Zhan, Y. Chen and M. Chen, *J. Energy Storage*, 2024, **86**, 111293.
20 Y. Luo, Y. Xie, H. Jiang, Y. Chen, L. Zhang, X. Sheng, D. Xie, H. Wu and Y. Mei, *Chem. Eng. J.*, 2021, **420**, 130466.
21 Q. Guo and Y. Tang, *Energy*, 2022, **241**, 122887.
22 A. Palacios, A. De Gracia, L. Haurie, L. F. Cabeza, A. I. Fernandez and C. Barreneche, *Materials*, 2018, **11**, 117.
23 A. H. Alkhazaleh, W. Almanaseer and A. Alkhazali, *Sustain. Energy Technol.*, 2023, **56**, 103059.
24 Z. M. Png, X. Y. D. Soo, M. H. Chua, P. J. Ong, J. Xu and Q. Zhu, *J. Mater. Chem. A*, 2022, **10**, 3633–3641.
25 Y. Su, Y. Fan, Y. Ma, Y. Wang and G. Liu, *Int. J. Therm. Sci.*, 2023, **185**, 108075.
26 X. Deng, C. Li, X. Sun, C. Wang, B. Liu, Y. Li and H. Yang, *Appl. Energy*, 2024, **368**, 123454.
27 Q. Zhang, L. Ma, T. Xue, J. Tian, W. Fan and T. Liu, *Composites, Part B*, 2023, **248**, 110377.
28 J. Niu, S. Deng, X. Gao, H. Niu, Y. Fang and Z. Zhang, *J. Energy Storage*, 2022, **47**, 103557.
29 H. Gu, C. Gao, A. Du, Y. Guo, H. Zhou, T. Zhao, N. Naik and Z. Guo, *J. Mater. Chem. C*, 2022, **10**, 2925–2937.

30 K. Tang, A. Zhang, T. Ge, X. Liu, X. Tang and Y. Li, *Mater. Today Commun.*, 2021, **26**, 101879.
31 I. Machado, C. Shaer, K. Hurdle, V. Calado and H. Ishida, *Prog. Polym. Sci.*, 2021, **121**, 101435.
32 Z. Deliballi, B. Kiskan and Y. Yagci, *Macromolecules*, 2020, **53**, 2354–2361.
33 Y. Wuliu, J. Liu, L. Zhang, S. Wang, Y. Liu, J. Feng and X. Liu, *Green Chem.*, 2021, **23**, 8643–8656.
34 S. Mahadik-Khanolkar, S. Donthula, C. Sotiriou-Leventis and N. Leventis, *Chem. Mater.*, 2014, **26**, 1303–1317.
35 Y. Xiao, L. Li, H. Cai, F. Liu, S. Zhang, J. Feng, Y. Jiang and J. Feng, *J. Appl. Polym. Sci.*, 2020, **138**, 50333.
36 X. Shen, L. Cao, Y. Liu, J. Dai, X. Liu, J. Zhu and S. Du, *Macromolecules*, 2018, **51**, 4782–4799.
37 S. Zhang, Z. Wang, Y. Hu, H. Ji, Y. Xiao, J. Wang, G. Xu and F. Ding, *Biomacromolecules*, 2022, **23**, 5056–5064.
38 X. Chen, H. Gao, Z. Tang, W. Dong, A. Li and G. Wang, *Energy Environ. Sci.*, 2020, **13**, 4498–4535.
39 Y. Xiao, L. Li, S. Zhang, J. Feng, Y. Jiang and J. Feng, *J. Mater. Sci.*, 2019, **54**, 12951–12961.
40 M. H. Zahir, S. A. Mohamed, R. Saidur and F. A. Al-Sulaiman, *Appl. Energy*, 2019, **240**, 793–817.
41 W. Aftab, J. Shi, M. Qin, Z. Liang, F. Xiong, A. Usman, S. Han and R. Zou, *Energy Storage Mater.*, 2022, **52**, 284–290.
42 N. Soodoo, K. D. Poopalam, L. Bouzidi and S. S. Narine, *Sol. Energy Mater. Sol. Cells*, 2022, **238**, 111650.
43 N. Soodoo, K. D. Poopalam, L. Bouzidi and S. S. Narine, *J. Energy Storage*, 2022, **51**, 104355.
44 Y. Lu, J. Liu, W. Zhao and K. Zhang, *Chem. Eng. J.*, 2023, **457**, 141232.
45 S. Mukherjee, N. Amarnath and B. Lochab, *Macromolecules*, 2021, **54**, 10001–10016.
46 H. Wang, Y. Deng, F. Wu, H. Jin, Y. Liu and J. Zheng, *Sol. Energy Mater. Sol. Cells*, 2021, **230**, 111236.
47 W. Luo, L. Luo, Y. Ma, Y. Liu, Y. Xie, X. Hu, W. Chen and X. Jiang, *J. Energy Storage*, 2024, **88**, 111583.
48 W. Luo, M. Zou, L. Luo, W. Chen, X. Hu, Y. Ma, Q. Li and X. Jiang, *ACS Appl. Mater. Interfaces*, 2022, **14**, 55098–55108.
49 J. Zhou, Y. Xiao, S. Liu, S. Zhang, Z. Li, C. Zhao, L. Li and J. Feng, *Adv. Colloid Interface Sci.*, 2024, 103185.
50 G. Kaya, B. Kiskan and Y. Yagci, *Macromolecules*, 2018, **51**, 1688–1695.
51 J. Liu, L. Zhang, X. Zhu, Q. Chen, K. Zhang and X. Liu, *ACS Appl. Polym. Mater.*, 2023, **5**, 6595–6606.
52 R. Lin, Y. Zhu, Y. Zhang, L. Wang and S. Yu, *Eur. Polym. J.*, 2018, **102**, 141–150.
53 S. K. Samanta, E. Preis, C. W. Lehmann, R. Goddard, S. Bag, P. K. Maiti, G. Brunklausd and U. Scherfa, *Chem. Commun.*, 2015, **51**, 9046–9049.
54 J. Dai, N. Teng, Y. Peng, Y. Liu, L. Cao, J. Zhu and X. Liu, *ChemSusChem*, 2018, **11**, 3175–3183.
55 X. Fan, S. Li, C. Wang, Y. Deng, C. Zhang and Z. Wang, *Eur. Polym. J.*, 2023, **187**, 111884.
56 Y. Qi, Z. Weng, Y. Kou, L. Song, J. Li, J. Wang, S. Zhang, C. Liu and X. Jian, *Chem. Eng. J.*, 2021, **406**, 126881.
57 Y. Lu, Y. Zhang and K. Zhang, *Chem. Eng. J.*, 2022, **448**, 137670.

